Impact against empty and water-filled X65 steel pipes – Experiments and simulations

Martin Kristoffersen[a,*], Folco Casadei[b], Tore Børvik[a], Magnus Langseth[a], Odd Sture Hopperstad[a]

[a] *Structural Impact Laboratory (SIMLab), Centre for Research-based Innovation (CRI), Department of Structural Engineering, Norwegian University of Science and Technology (NTNU), Rich. Birkelands vei 1A, NO-7491 Trondheim, Norway*

[b] *Retired from the European Laboratory for Structural Assessment (ELSA), Institute for the Protection and Security of the Citizen (IPSC), Joint Research Centre (JRC), 21027 Ispra, Italy*

Abstract

Offshore pipelines are frequently subjected to accidental impact loads, e.g. from anchors or trawl gear. A lot of parameters – including the pipe geometry, material properties, pipeline content, impact velocity, etc. – influence the course of such an impact. Some of these parameters have been studied quite extensively while others not so much. This study presents material and component tests on specimens taken from an X65 offshore pipeline. Empty pipes, as well as open and closed water-filled pipes, are impacted at different velocities. Results in terms of force-displacement curves are quite similar for the empty and open water-filled pipes, while the closed water-filled pipes react differently as a consequence of internal pressure build-up during impact. Computer simulations of the component tests are carried out using various numerical techniques for fluid discretisation and for fluid-structure interaction. Numerical results are generally in good agreement with experimental observations and serve as a helpful aid when interpreting results.

Keywords: Pipe impact tests, fluid-structure interaction, transient dynamics, SPH, Europlexus software

*Corresponding author, tel.: +47-73-59-46-87; fax: +47-73-59-47-01

1. Introduction

Pipelines are a crucial part of the offshore industry, widely used for distribution of oil and gas. Accidental loads can cause a great deal of trouble [1], and the pipelines' behaviour during and after being subjected to such loading scenarios is important to understand [2] as failure in a pipeline transporting oil and/or gas could have vast economical and environmental consequences. Det Norske Veritas (DNV) has published design guidelines on handling interference between pipelines and trawl gear [3], which allow for laboratory testing and advanced numerical simulations in addition to the simplified calculations provided therein. An elaborate list of accidental damage on structures in the North Sea and Norwegian Sea has been published by the Norwegian Petroleum Safety Authority (Ptil) [4].

Pipe impact problems have been studied with a lot of different approaches. Impact against fully clamped pipes have been studied by Jones et al. [5], and by Chen and Shen [6]. Addition of internal pressure to the pipe during impact was studied by Shen and Shu [7], by Ng and Shen [8] and more recently by Jones and Birch [9], who found a diffence in deformation between empty and pressurised pipes after impact. A lot fewer studies have been examining impact against liquid-filled pipes. Pipe perforation was by Neilson et al. [10] found to be more likely when water was present in the pipe during impact. These tests were performed at much higher impact velocities (46-325 m/s) than in the present study (< 5.2 m/s). Shah conducted experiments and simulations of simply supported water-filled copper pipes at a more relevant impact velocity (6.7 m/s) [11]. The pipes were 300 mm long with an outer diameter of 35 mm and wall thickness of 0.7 mm. Rubber membranes were mounted at the ends to restrain the water from escaping, thereby allowing pressure to build up inside the pipe. A difference between empty and water-filled pipes was observed post-impact, where the dent caused by the impact was confined to a smaller surface area of the pipe in the latter case. Similar results were obtained by Jones and Birch [9], in which pressurised pipes correspond to the water-filled pipes in [11]. A study focusing more on fracture in impacted pipes was conducted by Kristoffersen et al. [12]. In terms of numerical simulations, most work regarding pipes and fluid-structure interaction focuses on waterhammer

effects [13]. An analytical model for an impulse load against a pipe with a flowing medium has also been proposed [14]. A novel approach for estimating loads against pipelines due to trawl gear interaction has been suggested by Longva et al. [15].

This study presents impact tests against pipes made from an X65 grade offshore steel, and numerical simulations thereof. The effect of adding content (water) to the pipe was examined, with both open and closed ends. Adding water to an open pipe appeared to be negligible at the relatively low impact velocities of interest here, as the mass of the impactor is large compared to that of the pipe and water. Closing the pipe alters the force-displacement curve registered during impact, as pressure is allowed to build up inside the pipe. In the case of the highest impact velocity, the end cap ruptured in the weld as the pressure became too large. Furthermore, it was in the interest of this study to explore how different numerical techniques for fluid-structure interaction are able to handle such a problem. The impact experiments are generally well reproduced and the key phenomena are well captured by the computer simulations.

2. Material tests

The material used is an X65 grade offshore pipeline steel, the very same as used in [12]. It has a nominal yield stress of 450 MPa and an ultimate tensile strength of 535 MPa. Young's modulus is 208 000 MPa. All specimens for the material and component tests have been taken from the same continuous, seamless pipeline, which has an inner diameter of 123 mm and a nominal wall thickness of 9.5 mm. More details on the material can be found in [12].

2.1. Quasi-static uniaxial tension tests

Quasi-static uniaxial tension tests were performed on axisymmetric specimens as shown in Fig. 1. These tests are succinctly discussed here. The material was characterised as homogeneous across the cross-section (see Fig. 2(a)) based on tests carried out on specimens taken from different positions (north, south, east, west). Tests on specimens rotated 0°, 45° and 90° with respect to the pipe's longitudinal axis revealed isotropic behaviour (see Fig. 2(b)). A laser-based measuring device was used to continuously keep track of the

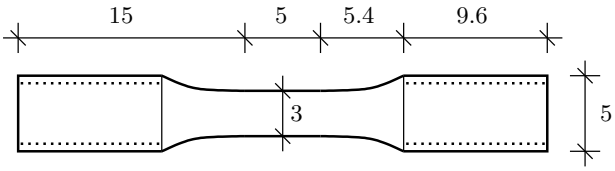

Figure 1: Specimen geometry for tensile tests. Dimensions in mm.

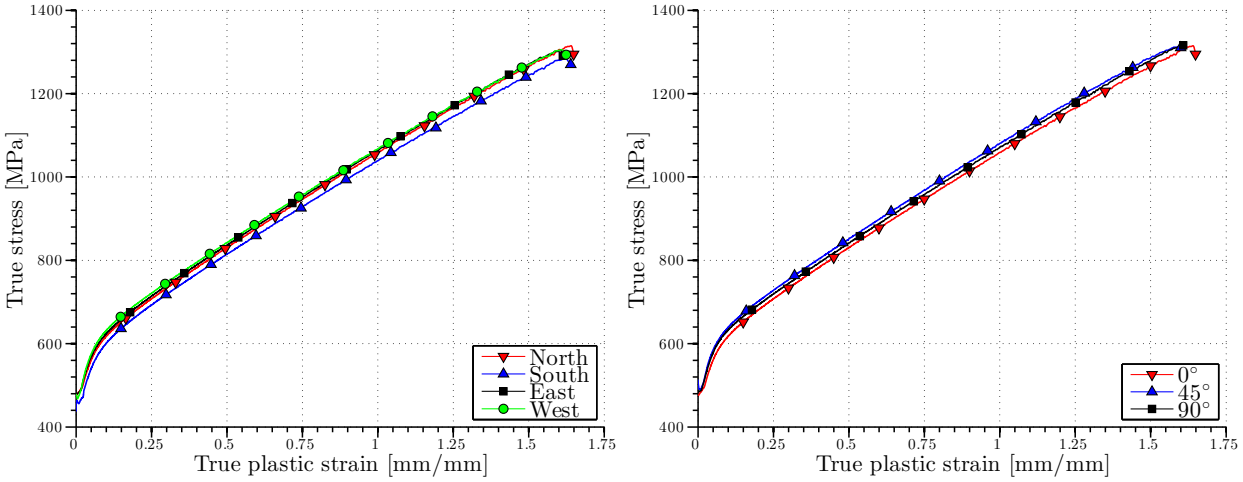

(a) Section homogeneity

(b) Isotropic behaviour

Figure 2: Data from quasi-static tensile tests on uniaxial specimens [12].

specimens' smallest diameter, allowing for calculation of true stress and true strain beyond necking. Based on values from 12 tests, the material yields at 478±15 MPa and has a nominal peak stress of 572 ± 14 MPa. It strain hardens to a true peak stress of $1\,314 \pm 12$ MPa and fails at a true strain of 1.61 ± 0.03 by a ductile cup-and-cone fracture.

2.2. Dynamic uniaxial tension tests

Impact is in general a dynamic problem, thereby nesessitating material data at elevated strain rates. Dynamic tensile tests on the specimen geometry in Fig. 1 were conducted in a split Hopkinson tension bar, the workings of which are described in [16]. Tests were carried out at three different strain rates, 240 s^{-1}, 535 s^{-1} and 830 s^{-1}. Two specimens were tested for each strain rate. As the material was already deemed homogeneous and isotropic [12], it did not matter from where and in which direction these specimens were taken, so they were all taken in the longitudinal direction of the pipe.

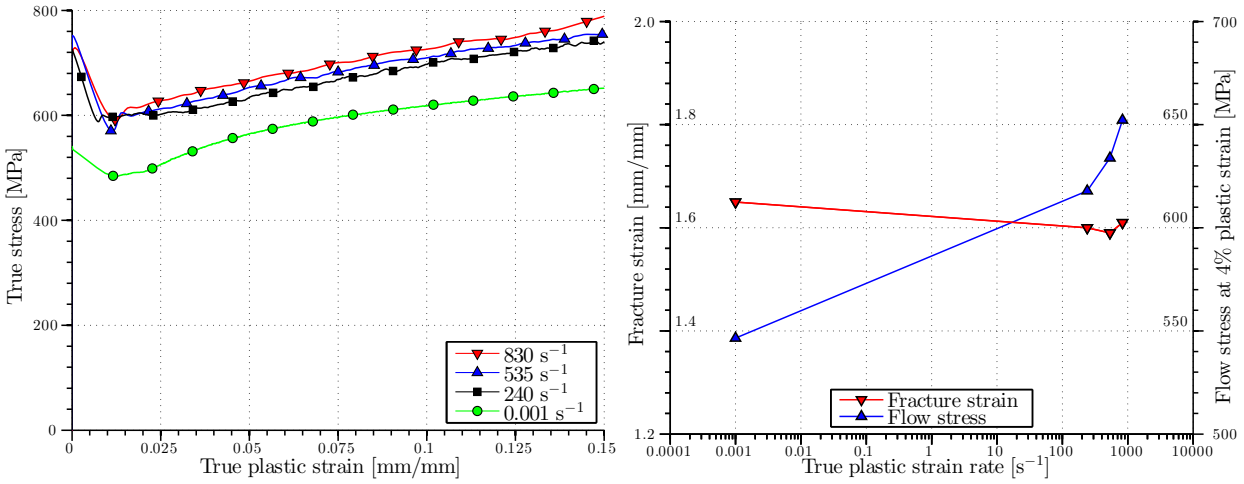

(a) True stress-true strain relation

(b) Fracture strain and flow stress

Figure 3: Data from dynamic tensile tests on uniaxial specimens.

An increase of flow stress is observed with increasing strain rate (shown in Fig. 3(a) in comparison with the quasi-static test), a common property of many metals. This is typically accompanied by a corresponding decrease of fracture strain, albeit not in this case. While the flow stress increased by about 20% (see Fig. 3(b)), the fracture strain ε_f – as calculated by $\varepsilon_f = \ln(A_0/A_f)$ where A_0 is the initial cross-sectional area and A_f is the cross-sectional area at fracture – remained of the same order as for the quasi-static tests (less than 1% alteration and within the standard deviation from the quasi-static tests). As material fracture is not considered in the present study, this observation is not followed up in detail at the current time. For more details on fracture in this material, see [12].

3. Component tests

3.1. Setup

The experimental setup of the component tests is the same as the impact part of the component tests conducted in [12], with a few modifications. A pendulum accelerator, meticulously described by Hanssen et al. [17], is used to launch a trolley of 1 472 kg into a simply supported pipe with a span of 1 000 mm, as shown in Fig. 4. Note that the pipes were mounted vertically in the test rig, with the open end/thin membrane facing up as seen

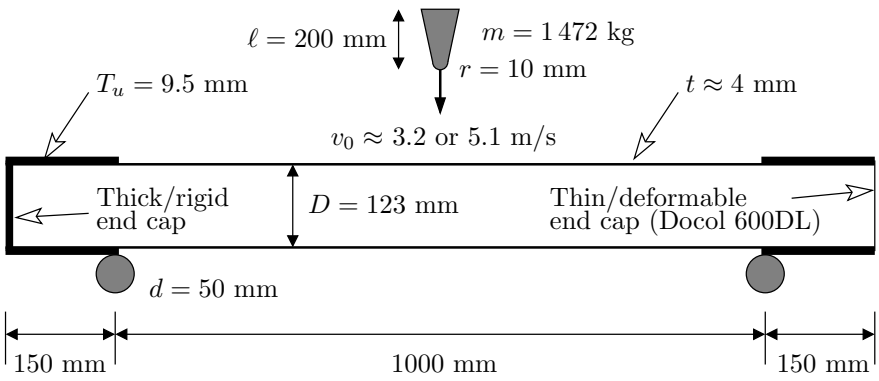

Figure 4: Setup of component tests (not to scale).

in Figs. 8 and 9.

The inner diameter of the pipe is 123 mm, and the thickness is lathed down from 9.5 mm to approximately 4 mm across the span, resulting in a D/t-ratio of about 30 which is common in many offshore pipelines [18]. Each pipe's resulting thickness was measured at different points (corresponding between the pipes) using a portable ultrasound device (see Table 1 for results). Empty pipes and water-filled pipes (open and closed) were tested at two different velocities, about 3.2 m/s and 5.1 m/s, making a total of six tests. The sharpest nose radius (10 mm) from the DNV guidelines [3] was chosen for the indenter. The contact force between the nose and the pipe was sampled using a 3-component load cell [19]. A complete test matrix, including results, can be found in Table 1.

For the water-filled pipes, end caps were used to contain the water. In the case of open pipes, only one end cap (the thick end, see Fig. 4) was used. One thick and one thin end cap were used for the closed pipes, thus limiting the bulging deformation to one end, which was filmed by a high-speed camera. Another high-speed camera filmed the global events. The initial pressure of the content in all pipes was atmospheric.

Based on the final deformation of the thin end cap it was possible, using some simple analytical expressions [20], to estimate a pressure p causing the measured deformation. The thick end cap had the same thickness and material as the unlathed section of the pipe, and was welded to the bottom end for a tight seal. A Docol 600DL steel plate of thickness 0.7 mm was welded to the top. This material was chosen as it is well studied and characterised in

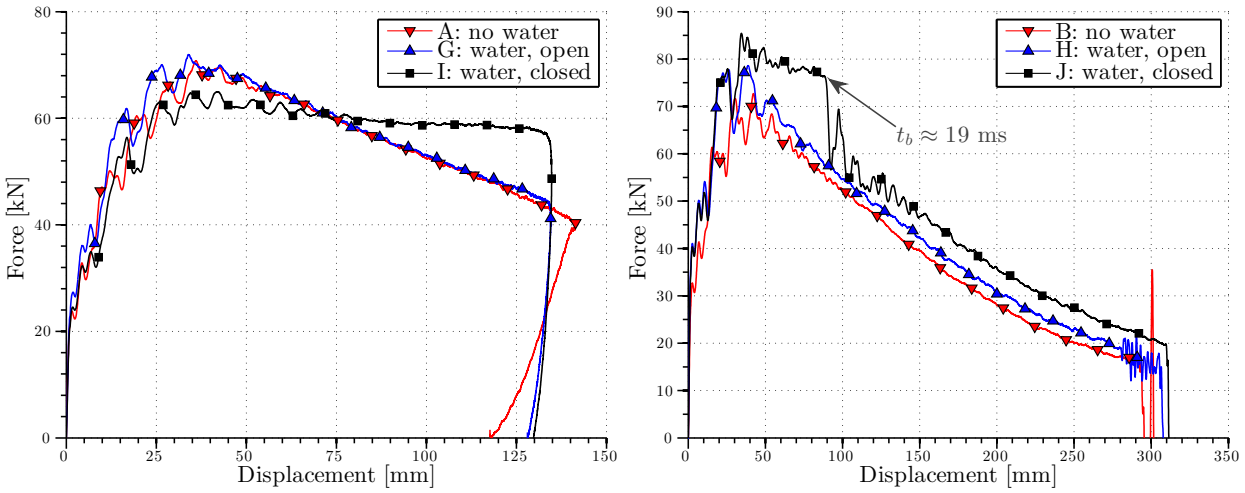

(a) Impact at ≈ 3.2 m/s

(b) Impact at ≈ 5.1 m/s

Figure 5: Force-displacement data from component tests.

previous works [21, 22]. As the top plate is at least one order of magnitude thinner than the thick end cap at the bottom, the bulging deformation is expected to take place at the top. Post-impact examination confirmed this assumption.

3.2. Results

Force-displacement curves for all tests are presented in Fig. 5, with part (a) showing impact at about 3.2 m/s and (b) impact at about 5.1 m/s. As seen, there is little difference in response between the empty pipes and the open pipes containing water. A slightly higher peak force is noted for the open water-filled pipes, but whether this is because of the added mass and inertia of the water, difference in thickness or local contact conditions, is hard to tell. Most likely it is a combination, which can be difficult to quantify.

At 3.2 m/s, the final global deformation was quite similar between the three cases, with the empty pipe having a somewhat larger deformation (see Fig. 6 for a typical outline of a deformed pipe). This can be attributed to the lower pipe wall thickness, and the inertia of the water (or rather, lack thereof). The trolley hit the buffer in the rig when testing at 5.1 m/s as the pipes were unable to absorb all the kinetic energy alone – hence the matching displacement at the end of the test.

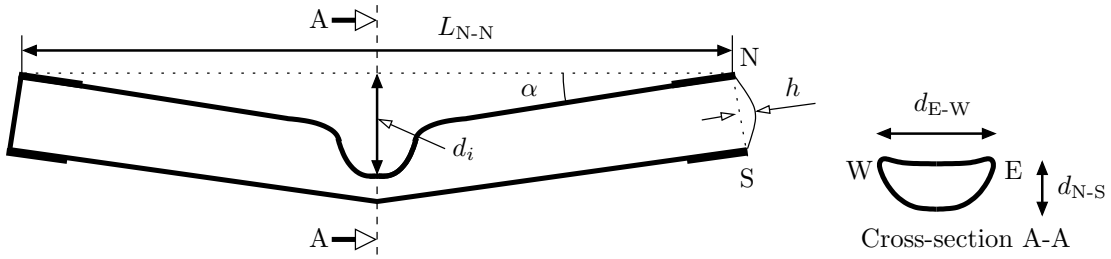

Figure 6: Typical outline of deformation shapes of pipes after impact load at midspan (not to scale), along with explanation of measurements given in Tables 1 and 3.

Table 1: Experimental matrix for component tests along with the impact test results. See Fig. 6 for measurement legend.

Pipe		**A**	**B**	**G**	**H**	**I**	**J**
Trolley mass	[kg]	1472	1472	1472	1472	1472	1472
Nose radius	[mm]	10	10	10	10	10	10
Avg. thickness	[mm]	3.89	3.86	4.08	4.06	4.02	4.16
		±0.36	±0.34	±0.21	±0.32	±0.23	±0.27
Water		No	No	Yes	Yes	Yes	Yes
End		Open	Open	Open	Open	Closed	Closed
Init. velocity	[m/s]	3.24	5.13	3.21	5.11	3.22	5.04
Kin. energy	[J]	7708	19356	7578	19245	7653	18713
Abs. energy*	[J]	7294	11736	6520	12880	12503	14710
Peak force	[kN]	70.7	72.7	71.9	78.6	65.0	85.4
d_i	[mm]	170	333	140	330	139	333
$L_{\text{N-N}}$	[mm]	1250	1104	1255	1095	1270	1103
$d_{\text{N-S}}$	[mm]	60	22	68	27	77	31
$d_{\text{E-W}}$	[mm]	180	199	174	198	168	198
α	[deg]	12	30	8	26	9	32

*Absorbed energy was estimated by integrating the measured force-displacement curve.

For the closed water-filled pipes, the force-displacement curve deviates strongly from the other two cases for both velocities. The force remained almost constant throughout the impact, and the pressure p was, based on the final end cap deformation, estimated to about 5.6 MPa after impact at 3.2 m/s. At the highest velocity, however, the weld attaching the thin end cap to the pipe ruptured and the water was no longer confined to remaining within the volume of the pipe, thereby resulting in a sudden drop in the force – indicated by an arrow in Fig. 5(b). The rupture happened after approximately 19 ms, as shown in Fig. 7, after which the force-displacement curve attained a similar shape to those of the empty pipe and the open water-filled pipe (albeit with a slightly higher force level, most likely due to the water being funneled through a narrow orifice).

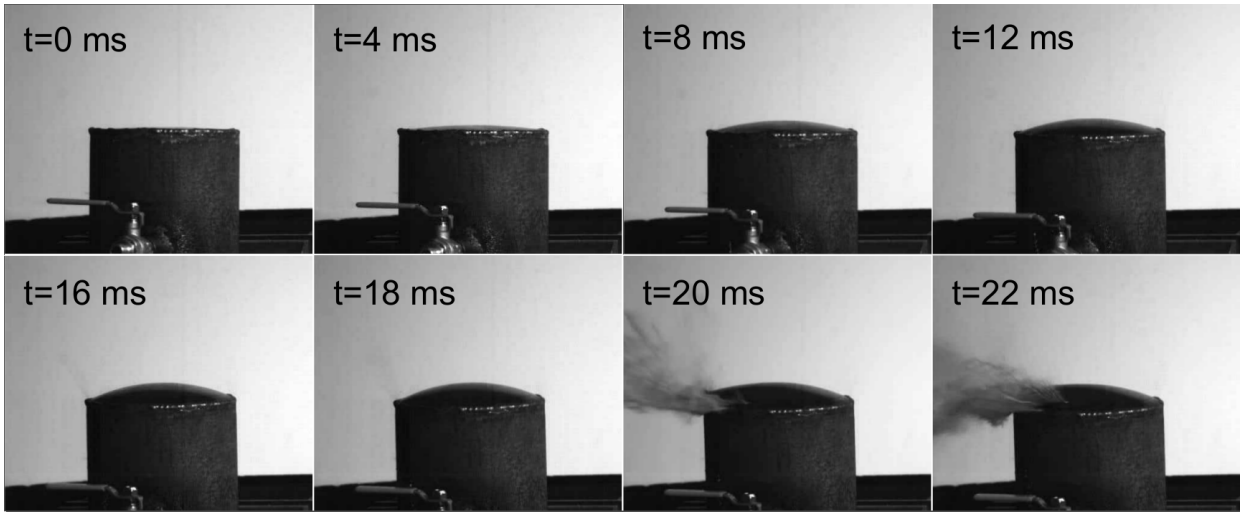

Figure 7: Pictures of top membrane on pipe J, taken by a high-speed camera.

Fig. 6 shows a sketch of a deformed pipe, including legends for the measurements given in Table 1. Frames of the global deformation from the high-speed video camera can be seen in Fig. 8 (3.2 m/s) and Fig. 9 (5.1 m/s).

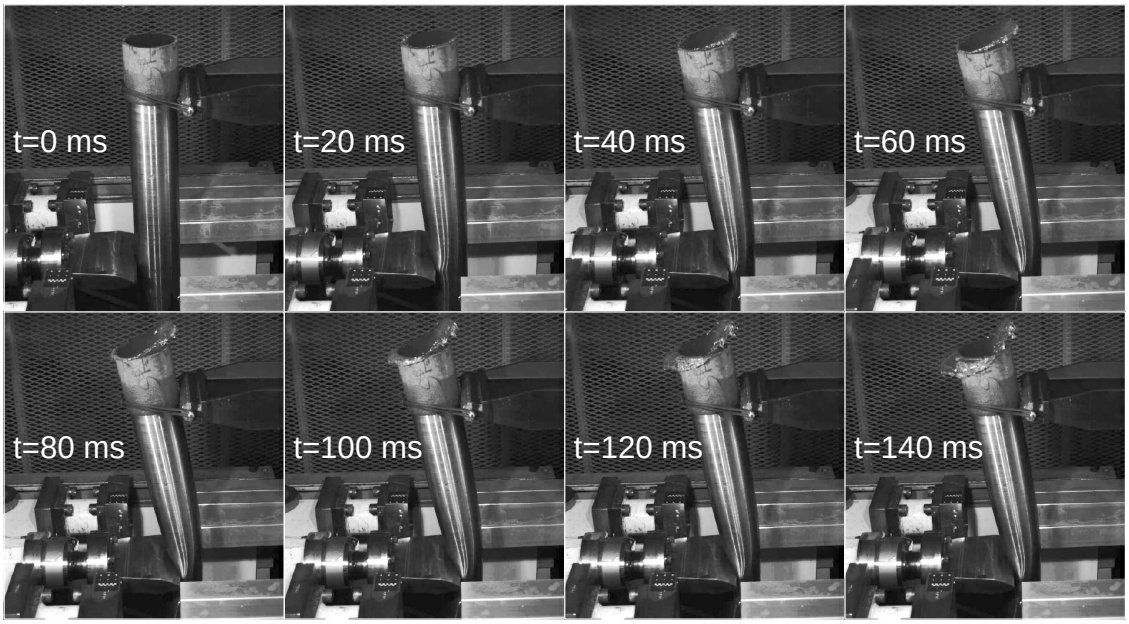

(a) Images from high-speed video of impact against pipe G ($v_0 = 3.21$ m/s)

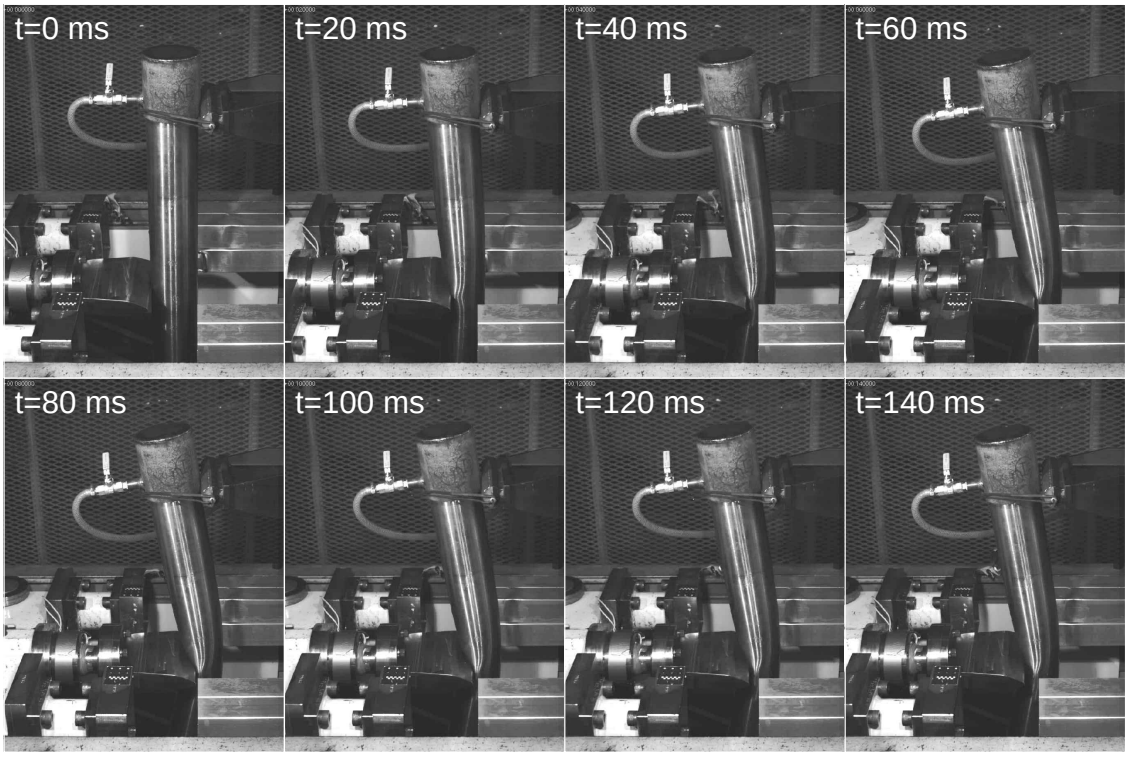

(b) Images from high-speed video of impact against pipe I ($v_0 = 3.22$ m/s)

Figure 8: Images from component tests at medium velocity (≈ 3.2 m/s).

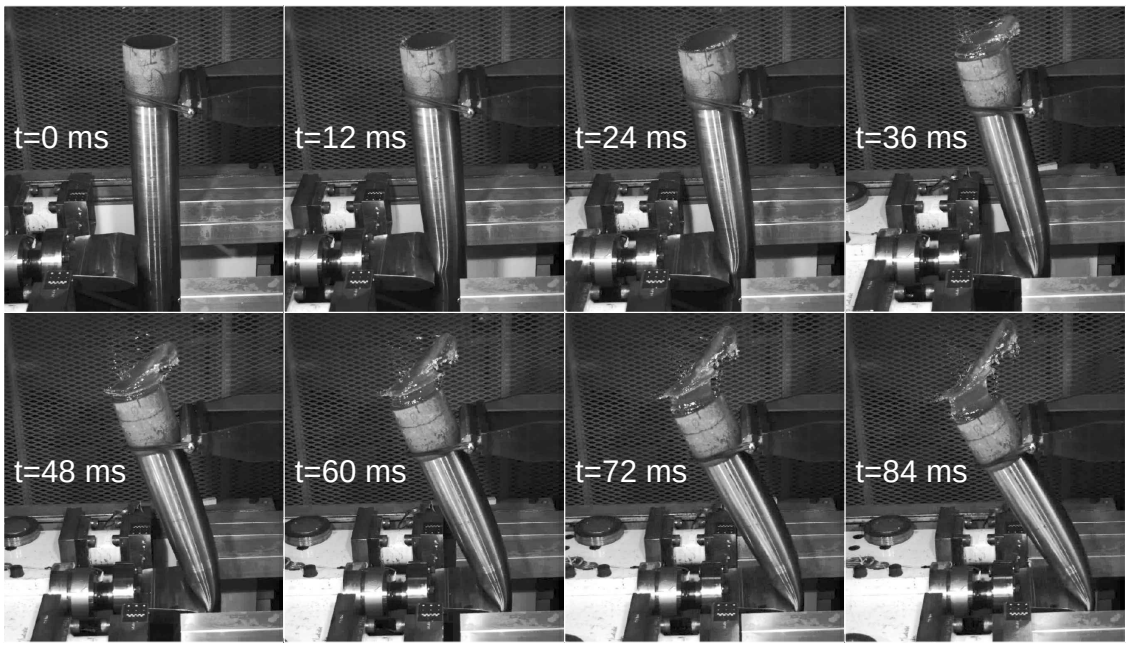

(a) Images from high-speed video of impact against pipe H ($v_0 = 5.11$ m/s)

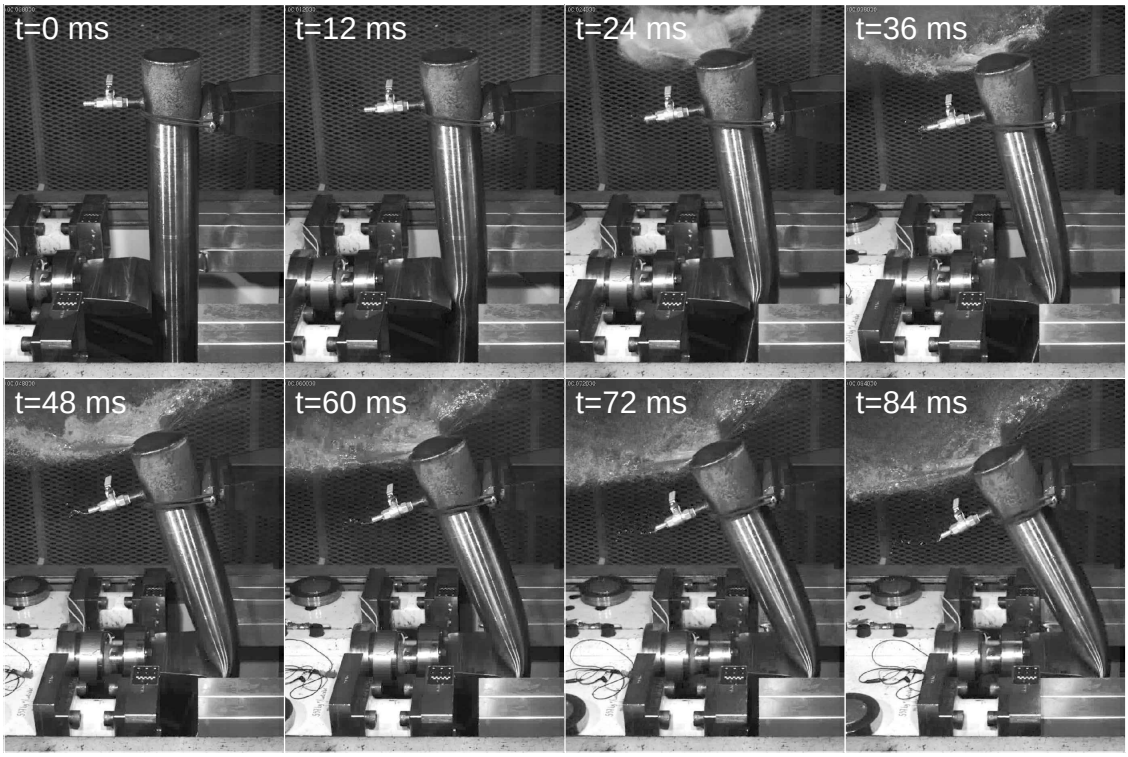

(b) Images from high-speed video of impact against pipe J ($v_0 = 5.04$ m/s)

Figure 9: Images from component tests at high velocity (≈ 5.1 m/s).

4. Material models

4.1. Constitutive relations

X65 pipeline steel

The X65 pipeline material has been modelled using the Johnson-Cook (JC) constitutive relation [23]. It accounts for isotropic hardening, strain rate sensitivity and thermal softening. The von Mises yield criterion is used with the associated flow rule, where the von Mises equivalent stress σ_{eq} is a function of the deviatoric part $\boldsymbol{\sigma}^{\mathrm{dev}}$ of the Cauchy stress tensor $\boldsymbol{\sigma}$,

$$\sigma_{\mathrm{eq}}\left(\boldsymbol{\sigma}\right) = \sqrt{\frac{3}{2}\boldsymbol{\sigma}^{\mathrm{dev}} : \boldsymbol{\sigma}^{\mathrm{dev}}} \tag{1}$$

The JC flow stress σ_{JC} is expressed as

$$\sigma_{\mathrm{JC}}\left(\varepsilon_{\mathrm{eq}}, \dot{\varepsilon}^{*}_{\mathrm{eq}}, T^{*}\right) = \left(A + B\varepsilon^{n}_{\mathrm{eq}}\right)\left(1 + C\ln\dot{\varepsilon}^{*}_{\mathrm{eq}}\right)\left(1 - T^{*m}\right) \tag{2}$$

where $\varepsilon_{\mathrm{eq}}$ is the equivalent plastic strain, and A, B, n, C and m are material constants. The dimensionless plastic strain rate is given by $\dot{\varepsilon}^{*}_{\mathrm{eq}} = \dot{\varepsilon}_{\mathrm{eq}}/\dot{\varepsilon}_{0}$, where $\dot{\varepsilon}_{0}$ is a user-defined reference strain rate, which here is taken as the minimum plastic strain rate for which material tests have been done. Strain rates below this threshold are treated as static.

The homologous temperature is defined as $T^{*} = (T - T_r)/(T_m - T_r)$, where T is the absolute temperature, T_r is the ambient temperature and T_m is the melting temperature of the material. This problem is assumed to be isothermal, thus omitting the temperature bracket of Eq. (2) and thereby reducing it to

$$\sigma_{\mathrm{JC}}\left(\varepsilon_{\mathrm{eq}}, \dot{\varepsilon}_{\mathrm{eq}}\right) = \left(A + B\varepsilon^{n}_{\mathrm{eq}}\right)\left(1 + C\ln\frac{\dot{\varepsilon}_{\mathrm{eq}}}{\dot{\varepsilon}_{0}}\right) \tag{3}$$

Then, from Eq. (1) and Eq. (3), the dynamic yield function f_{JC} becomes

$$f_{\mathrm{JC}}\left(\boldsymbol{\sigma}, \varepsilon_{\mathrm{eq}}, \dot{\varepsilon}_{\mathrm{eq}}\right) = \sigma_{\mathrm{eq}}\left(\boldsymbol{\sigma}\right) - \sigma_{\mathrm{JC}}\left(\varepsilon_{\mathrm{eq}}, \dot{\varepsilon}_{\mathrm{eq}}\right) \tag{4}$$

The initial size of the yield surface, i.e. when the equivalent plastic strain is zero, is given by the constant A. Implementation of the model into Europlexus is described in [24].

Docol 600DL

For the deformable end cap made from 0.7 mm thick Docol 600DL plates, a piecewise linear (PL) isotropic von Mises material was used with the associated flow rule. The equivalent stress is as expressed in Eq. (1), and the flow stress is extracted from tabulated data making the yield function

$$f_{\mathrm{PL}}\left(\boldsymbol{\sigma}, \varepsilon_{\mathrm{eq}}\right) = \sigma_{\mathrm{eq}}\left(\boldsymbol{\sigma}\right) - \sigma_{\mathrm{PL}}\left(\varepsilon_{\mathrm{eq}}\right) \tag{5}$$

The deformation and plastic strains in the Docol 600DL end cap are small compared to those of the X65 pipes, leading to the assumption that the strain rates are low as well – of the order of 10 s^{-1} and below. This material has been shown to have negligible strain rate effects at such low strain rates and levels of plastic strain [22], thereby justifying the omission of viscoplastic effects in the end cap.

4.2. Identification of material constants for X65 steel

To determine the equivalent stress σ_{eq} from the (true) measured major principal stress σ_1 after necking, Bridgman's analysis [25] was employed

$$\sigma_{\mathrm{eq}} = \frac{\sigma_1}{\left(1 + \frac{2R}{a}\right) \cdot \ln\left(1 + \frac{a}{2R}\right)} \tag{6}$$

The relation between the radius of the specimen's cross-section at the root of the neck, a, and the radius of the neck profile, R, was estimated by the empirical relation proposed by Le Roy et al. [26]

$$\frac{a}{R} = 1.1 \cdot \left(\varepsilon_{\mathrm{eq}} - \varepsilon_U\right) \tag{7}$$

valid for $\varepsilon_{\mathrm{eq}} > \varepsilon_U$ where ε_U is the equivalent plastic strain at the onset of necking. Material data from Figs. 2 and 3 were then used to calibrate the JC model in Eq. (3), by using a least squares fitting. Fracture was not accounted for in this study as the global response was the main topic of interest. Material constants used for the JC model can be found in Table 2.

Data for the Docol 600DL steel was obtained from [21], where a Voce model was fitted to experimental data. A total of 100 points equidistant on the equivalent strain axis were taken from this model and entered into Europlexus as tabulated data.

Table 2: Material constants for JC model of X65 steel.

Elasticity and density		
E [MPa]	ν	ρ [kg/m^3]
208 000	0.33	7 800

Yield stress, strain hardening		
A [MPa]	B [MPa]	n
465.5	410.8	0.4793

Strain rate effect	
$\dot{\varepsilon}_0$ [s^{-1}]	C
0.000806	0.0104

5. Numerical modelling

Simulations of the experiments described in Section 3 are conducted using the explicit finite element code Europlexus [27], which is developed jointly by Joint Research Centre (JRC) in Ispra, Italy, and by the French Commissariat à l'Energie Atomique (CEA) for fast transient dynamics involving fluid-structure interaction (FSI).

The fluid domain is modelled by the Euler equations, assuming compressible inviscid behaviour. Finite Elements (FE), cell-centred Finite Volumes (FV) or Smoothed Particle Hydrodynamics (SPH) were employed here for the fluid discretisation in space. Yet another fluid formulation based on node-centred Finite Volumes is available in the code, but was not used in the present study. Europlexus offers a rich variety of FSI models, as described in [28]. Conforming, non-conforming or embedded (immersed) meshes can be employed. The enforcement of FSI conditions can be achieved either in a strong manner (typical of FE) by means of Lagrange multipliers to impose velocity constraints, or in a weak manner (typical

of cell-centred FV), by transmitting pressure forces. The general setup of the numerical simulations is as presented in Fig. 4.

5.1. Structure model

An appropriate Lagrangian finite element discretisation of the pipe was obtained in [29], where $24 \times 78 = 1\,872$ elements were used (24 along the circumference and 78 along the length as shown in Fig. 10), making the element edges about 16 mm long. The elements are 4-node shells with 6 degrees of freedom per node, and 20 Gauss points (5 across the thickness). In addition, 180 such elements were used to model each end cap. This structural mesh is referred to as "medium" and used as a basis mesh for the pipe in the simulations. Other mesh grades were also used, coarse (16×52), fine (32×104) and extra fine (40×130).

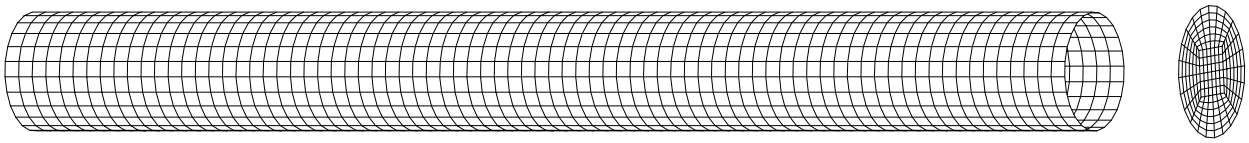

Figure 10: Medium mesh for pipe (24×78 elements) and end caps (180 elements).

Both the supports and the indenter were represented by 40 material points (rigid spheres) each, thereby approximating a cylinder. The pinball contact algorithm, originally proposed by Belytschko and co-workers for impact and penetration problems with erosion (see [30] and references therein), was used to enforce the contact conditions. The method does not account for friction, and works by embedding a rigid sphere (pinball) in each element candidate for contact. Then, contact detection reduces to checking interpenetration of two spheres, a trivial and geometrically robust operation which by construction avoids the pitfalls of other detection algorithms, e.g. based on master nodes penetrating into slave surfaces.

The supports were assigned pinballs of radius 25 mm, and the indenter's pinball radius was set to 10 mm (see Fig. 4). Indeed, these components are represented quite accurately by spherical pinballs. However, as concerns the pipe, quadrilateral shell elements would be only poorly represented by spheres, so two alternative strategies were tested. In some cases, node-based (rather than element-based) pinballs with a diameter equal to the shell

thickness were also assigned to all shell nodes of the pipe in the impact zones. Alternatively, a "hierarchic" pinball technique (also initially proposed by Belytschko) was used in the pipe, which starts with a pinball size approximately equal to the shell's length and is subsequently reduced to the order of the shell thickness as contact progresses. The difference in behaviour between the two contact formulations will be shown in Fig. 13. The supports are fixed in all spatial directions while the indenter is only allowed to move in the impact direction, thus representing the nose of the trolley which in the experiments is limited to travelling along the rails in the pendulum accelerator.

5.2. Fluid model and FSI

The fluid inside the pipe in experiments G, H, I and J is discretised in various different manners, and the FSI technique varies accordingly. Three main variations of representing the fluid are employed in the present work: *i*) by an arbitrary Lagrangian-Eulerian (ALE) mesh of either FE or FV; *ii*) by a completely Eulerian mesh of either FE or FV; *iii*) by smoothed-particle hydrodynamics (SPH). As in the experiments, all fluids' initial pressure is atmospheric (approximately 10^5 Pa).

ALE approach

In the first case, the end cap mesh seen in Fig. 10 is extruded along the pipe's longitudinal axis to create linear 8-node volume elements containing one Gauss point located at the centre. For a conforming fluid mesh – i.e. a mesh with one corresponding fluid node for each structural node on the fluid-structure interface and vice versa – this results in $180 \times 78 = 14\,040$ elements for the medium structural mesh. A finer fluid discretisation would give a non-conforming fluid mesh, with one corresponding fluid node for each structural node on the F-S interface albeit not the other way round. Making the fluid coarser than the structure is not advisable.

Since the fluid mesh is situated inside the pipe it must necessarily deform along with the pipe, necessitating a reasonable rezoning procedure for the mesh. Giuliani's automatic mesh rezoning algorithm [31] was employed with success in most calculations. In the cases with highest deformation of the pipe, an alternative specialised rezoning model based upon

homeomorphic deformation gave slightly better results. Nodes on the F-S interface are constrained to move along with the associated structure nodes in all spatial directions.

For FE in the fluid, the FSI model of choice in the classical ALE approach, whereby the fluid mesh moves and deforms along with the structure mesh, is the so-called FSA model described in [32]. It works with conforming as well as non-conforming [33] fluid-structure meshes.

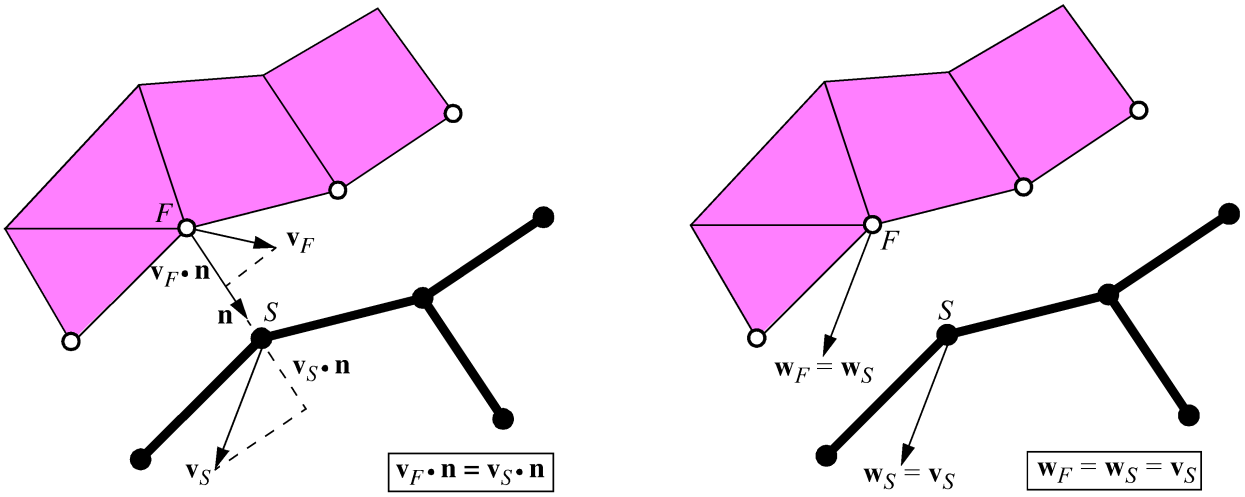

(a) Constraint on particles velocity

(b) Compatibility of mesh velocities

Figure 11: Fluid-structure interaction by the FSA algorithm.

According to the FSA algorithm (and restricting ourselves to the conforming case for simplicity), any fluid node F on the F-S interface (see Fig. 11(a)) is subjected to a restriction: the fluid velocity at this node, $\mathbf{v}_F$, is constrained (by a Lagrange multipliers method, dubbed the "strong" approach) to be equal to the structure velocity $\mathbf{v}_S$ at the corresponding structural node S, along the unit normal to the F-S interface $\mathbf{n}$, i.e.

$$\mathbf{v}_F \cdot \mathbf{n} = \mathbf{v}_S \cdot \mathbf{n} \tag{8}$$

As concerns the mesh velocity $\mathbf{w}$, which is arbitrary in ALE, the following condition is imposed (see Fig. 11(b)),

$$\mathbf{w}_F = \mathbf{w}_S \tag{9}$$

ensuring that the structure and the fluid meshes move and deform together. The FSA algorithm is relatively simple and very accurate, but is limited to cases whereby the fluid mesh deformation is not excessive and the structure deforms but does not fail.

For cell-centred FV in the fluid, the velocity is not discretised at nodes but at the cell centres. In this case, FSI is achieved in a "weak" manner by transmitting pressure forces from the fluid to the neighbouring structure, see [28] for details.

Since only one type of fluid (the water inside the pipe) is modelled, at least in the cases of closed filled pipes, the classical ALE approach requires just a standard, single-component material model for the water (although it can be extended to a multi-phase multi-component material model).

Euler-Lagrange approach

In the second case, the structure and fluid meshes are built independently. The Lagrangian structure mesh is then "embedded" or "immersed" in a regular, parallelepiped Eulerian fluid mesh which represents the fluid domain both inside (water) and outside (air) the pipe. In the present calculations, a block of $60 \times 36 \times 180 = 388\,800$ fluid bricks was used, measuring $500 \times 300 \times 1\,500$ mm. Absorbing boundaries are specified along the entire envelope of the fluid domain in order to avoid spurious reflections of pressure waves along the mesh boundaries.

This approach requires a multi-phase multi-component material model for the fluid domain, able to represent an arbitrary mixture of liquid water and air. Such models are more complex and less accurate than single-component models. The tracking of interfaces between the phases is less precise and subjected to numerical diffusion. However, as a counterpart, all difficulties related to mesh rezoning are avoided by construction, since the fluid mesh is Eulerian (fixed). For FE in the fluid, coupling between the fluid and the structure is achieved by the so-called FLSR algorithm explained briefly below. See [28, 34] for further details.

To determine which fluid nodes participate in the FSI, a sphere with a given radius (large

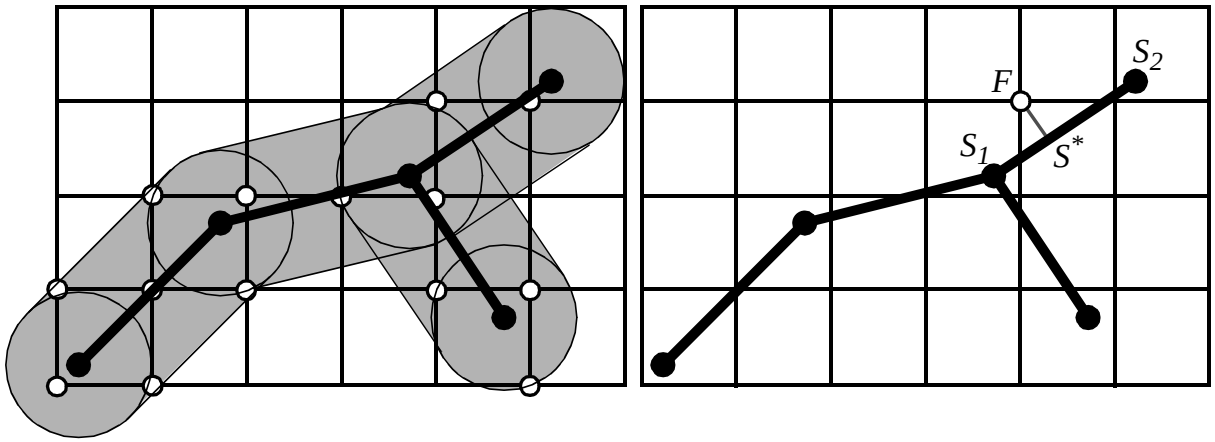

(a) Influence domain (shaded) (b) Fluid-structure coupling

Figure 12: Fluid-structure interaction by the FLSR algorithm.

enough to include some fluid nodes, but not too many) is placed on each structural node. The spheres are then connected via prisms, cones and hexahedra, creating a certain volume around the structure, called the "influence domain" and illustrated in 2D in Fig. 12(a). All fluid nodes within the influence domain participate in the FSI. As the calculation progresses and as the structure moves and deforms, this domain has to be continuously updated. To keep the computational cost acceptable, fast search algorithms for the identification of the current FSI nodes are employed.

According to the FLSR algorithm, any fluid node F inside the domain (see Fig. 12(b)) is subjected to a restriction: the fluid velocity $\mathbf{v}_F$ at this node is constrained (by a Lagrange multipliers method: strong approach) to be equal to the structure velocity $\mathbf{v}_{S^*}$ at the closest point S^*, along the unit normal to the structure $\mathbf{n}_S$, i.e.

$$\mathbf{v}_F \cdot \mathbf{n}_S = \mathbf{v}_{S^*} \cdot \mathbf{n}_S = (N_1 \mathbf{v}_{S_1} + N_2 \mathbf{v}_{S_2}) \cdot \mathbf{n}_S \tag{10}$$

in which N_1 and N_2 are the shape functions of the structural element containing S^*. This attempts to leave the fluid free to slide along the structure tangentially, while it cannot pass through the structure in its normal direction. Another alternative would be to tie the fluid velocity to the structure velocity along all spatial directions, i.e.

$$\mathbf{v}_F = \mathbf{v}_{S^*} = N_1 \mathbf{v}_{S_1} + N_2 \mathbf{v}_{S_2} \tag{11}$$

This has the advantage of hindering potential numerical fluid leakage (spurious passage of fluid across the structure) while it may tie the fluid too strongly to the structure, thereby causing some unphysical loading along the structure's tangential direction as more mass has to be moved during motion. The form in Eq. (10) or Eq. (11) can be chosen by choosing the fluid-structure coupling parameter (FSCP) equal to 0 or 1, respectively, in the input file.

For cell-centred FV in the fluid domain, the weak variant of the embedded algorithm, named FLSW, is used. Fluid volume *interfaces* are tracked when determining the influence domain rather than fluid nodes (see [28] for details). The embedded FLSR/FLSW algorithm is less accurate and more CPU-time consuming than the classical FSA algorithm, but it is much more general. It lends itself well to extreme motion and deformation of the structure, which can even undergo failure and fragmentation.

In the present Euler-Lagrange simulations the impactor has been left out of the FSI scheme for simplicity, since it only serves as a means for delivering the kinetic energy to the pipe.

SPH approach

In the third and final case, the fluid is modelled by classical SPH particles, all of the same size and initially arranged in a densely packed (hexagonal close-packed) configuration, only approximately filling the pipe. The fluid description is Lagrangian in this case, and it lends itself well to the treatment of impacts. There is no additional difficulty to model a partially filled pipe and the fragmentation or jetting of the water is naturally described. For an introduction to SPH including derivation of the SPH equations, see [35].

In the present calculations a radius of the SPH particles of 2.5 mm is chosen. To fill the entire pipe 169 971 particles are needed. Fluid-structure interaction in this case reduces to Lagrangian contact between the SPH particles and the shell elements of the pipe.

6. Numerical results

This section summarises the results of the numerical simulations performed with the various models. The main focus has been with pipes A and I, as they showed a distinctly different behaviour in the experiments (in terms of force-displacement) and there was no failure of the material (which was the case for pipe J). The results emerging from the simulations have been sorted according to the numerical technique used, and not according to the pipe experiments.

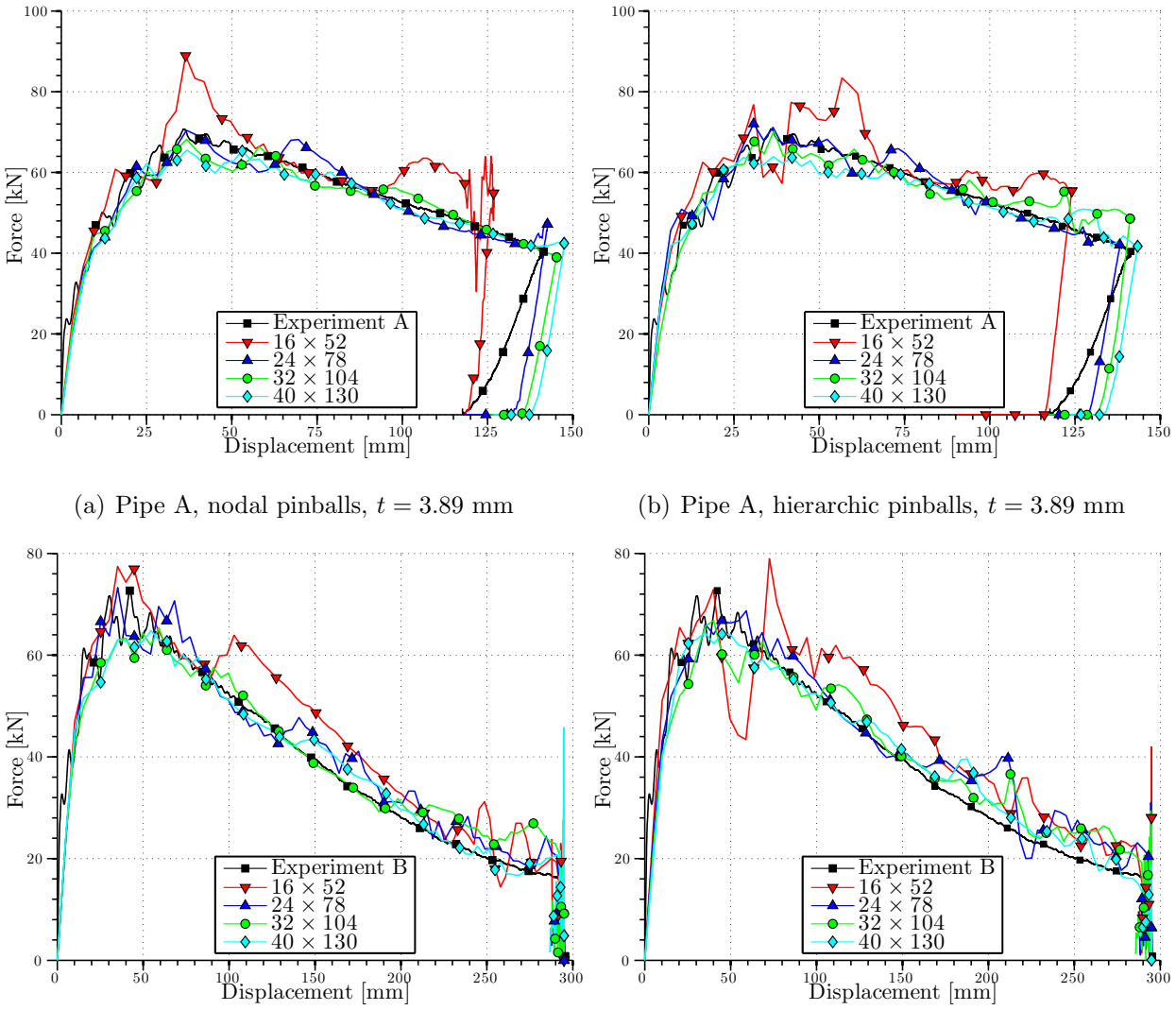

(a) Pipe A, nodal pinballs, $t = 3.89$ mm

(b) Pipe A, hierarchic pinballs, $t = 3.89$ mm

(c) Pipe B, nodal pinballs, $t = 3.86$ mm

(d) Pipe B, hierarchic pinballs, $t = 3.86$ mm

Figure 13: Mesh and contact model sensitivity study on empty pipes.

6.1. Empty pipe simulations (Lagrangian)

Despite having an appropriate mesh density from previous work [29], a few simulations with different mesh grades were run. The coarse mesh did not perform satisfactorily, and a converging tendency was observed for increasing number of elements, as seen in Fig. 13. More elements also tended to generate a softer behaviour, which is natural as more degrees of freedom are available and the system is less "restrained".

Different shell thicknesses were tried out numerically for the pipe due to the mid section being lathed down in the experiments, which resulted in a slightly uneven thickness and a slightly different average thickness for each pipe. A higher thickness lead to a higher force level and correspondingly lower deformation, illustrated in Fig. 14. This also conforms with expectations, as higher thickness should provide a stiffer response.

No significant difference between nodal and hierarchic pinballs was observed, except for the case with the coarse mesh where the nodal pinballs simply were too far apart to ensure sufficient contact conditions (see Fig. 13). For pipe B, the final deformation is equal for all analyses as the trolley hit the buffer in the experiment. This buffer was also included in the analyses as a rigid barrier the indentor could not pass, hence the clutter of data points at the end of the analyses. The impact was well captured, and in accordance with previous work [36] using ABAQUS/Explicit to perform the numerical simulations of empty pipes.

6.2. Conforming ALE simulations of filled pipe

A conforming mesh for the fluid was constructed within the pipe, and a simulation was set up for comparison with experiment I. All initial simulations (using the different discretisations) with a pipe completely filled with water showed that the response was much too stiff (see e.g. Fig. 15). Therefore, it was suspected that in the nominally filled-closed tests (I, J) some air could have remained trapped at the tube top, since the filling tap was not at the highest point (see Figs. 8(b) and 9(b)).

To check this conjecture, the effect of increasing the air content in the pipe was investigated by using a multi-phase multi-component material model allowing for a mixture of air and water. For each mesh density, the top layer of elements was modelled as air. Increasing

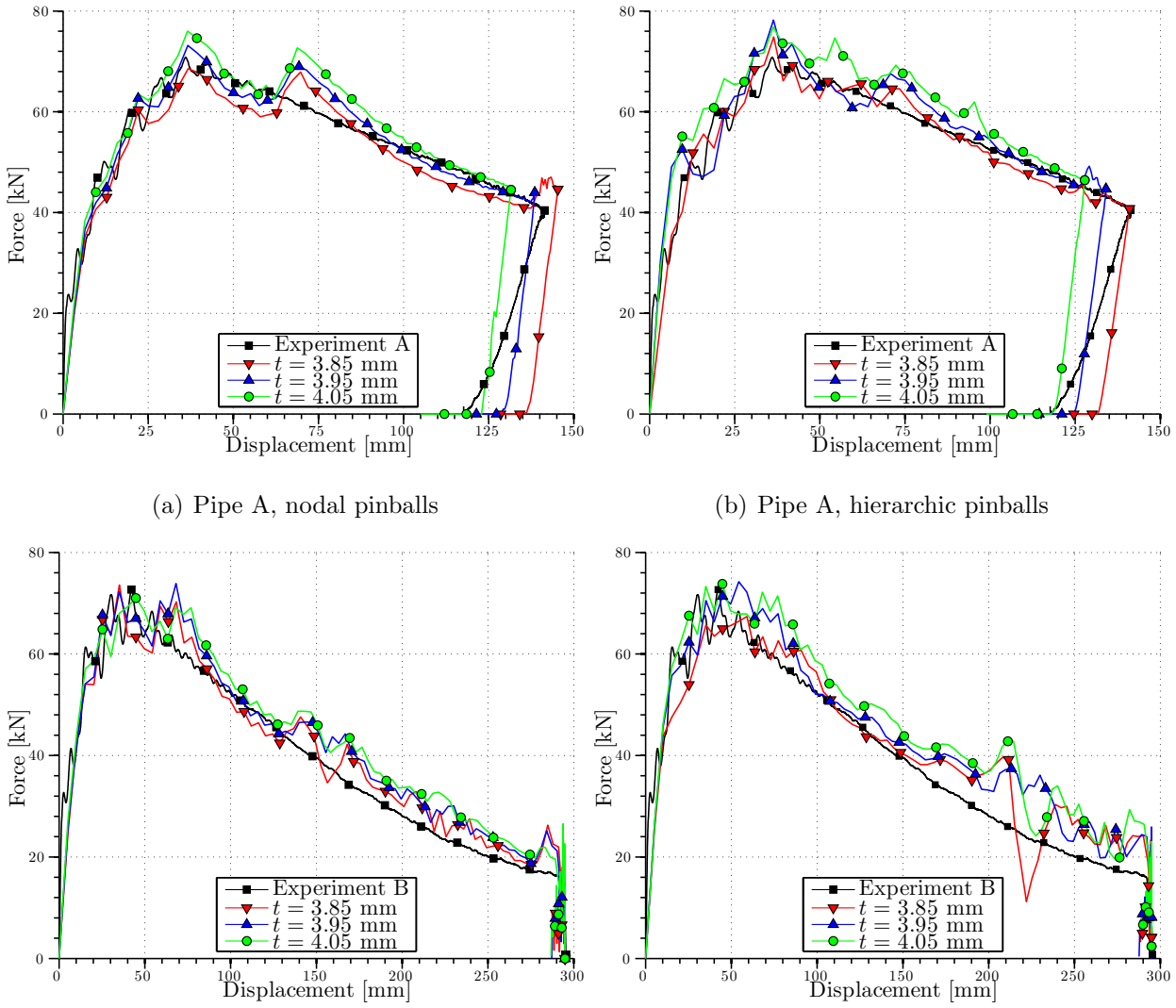

(a) Pipe A, nodal pinballs

(b) Pipe A, hierarchic pinballs

(c) Pipe B, nodal pinballs

(d) Pipe B, hierarchic pinballs

Figure 14: Thickness and contact model sensitivity study on empty pipes, medium mesh density (24×78).

the air content successively to two and three rows of elements showed that higher air content changed the behaviour towards that of an open water-filled or empty pipe, which is what one would expect in practice as well. This is the case for all mesh densities, and one row of elements with air has a greater influence on the medium mesh (Fig. 15(a)) compared to, say, the extra fine mesh (Fig. 15(c)). One row in the medium mesh is approximately 19.2 mm, while in the extra fine mesh one row is about 11.5 mm. So it seems that to obtain a flatter force-displacement curve as seen in the experiments, it is crucial to have the correct fraction

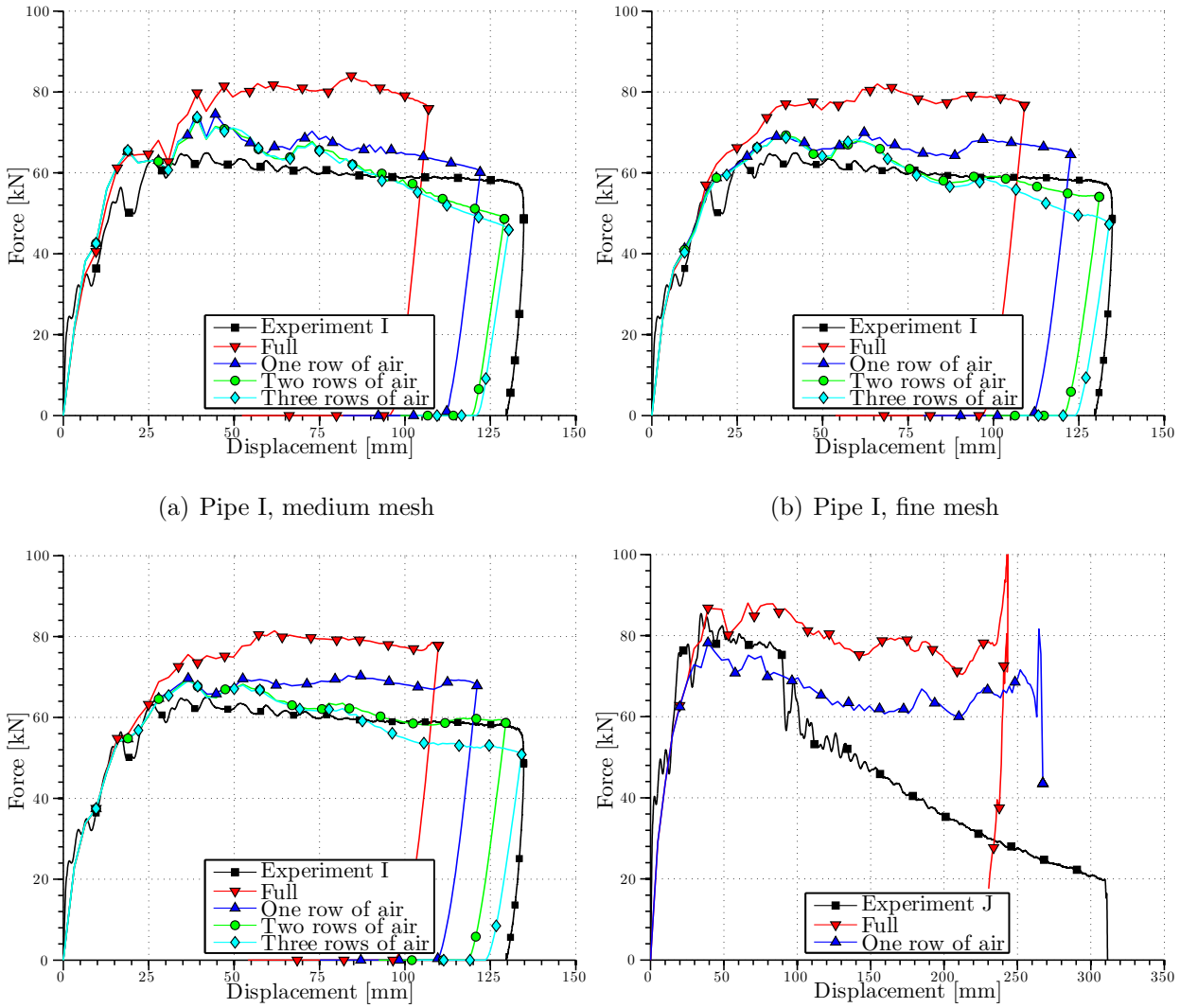

(a) Pipe I, medium mesh

(b) Pipe I, fine mesh

(c) Pipe I, extra fine mesh

(d) Pipe J, medium mesh

Figure 15: Simulations of closed, water-filled pipes (experiments I and J).

of air trapped in the pipe so that pressure builds up accordingly. After this consideration, a rather good match with the experimental data is acquired. It is worth noting that the stiffness of the test, i.e. the initial tangent of the force-displacement curves, is well captured in all simulations as this part takes place before any significant rise of pressure (the change of volume is still small at this point).

The same setup with a medium mesh was applied to pipe J, the closed water-filled pipe impacted at 5.1 m/s. In the experimental case the weld attaching the end cap failed

after about 19 ms (and deformation of approximately 90 mm, as seen in Fig. 5(b)), and since fracture is unaccounted for in the present study, results beyond this point would be inaccurate at best. From Fig. 15(d), it can be seen that results are quite decent until the point of failure. The simulation with a completely full pipe has a higher peak force and force level throughout the analysis compared to the experiment and the simulation with one row of air at the top. This second simulation has a force-displacement curve slightly below the experimental, suggesting that the air content is somewhat less than one row of elements in this case.

A refined mesh should be tested with the same setup for pipe J, but this was not explored in more detail as a proof of concept for this approach is shown for pipe I. Besides, no fracture criterion is employed at the moment, rendering further analyses somewhat redundant. Despite smooth-looking curves, the simulations of pipe J did have some instabilities due to excessive distortion of the cross-section, and Giuliani's rezoning algorithm [31] succeeded in keeping the mesh in the impact zone from becoming warped. The analyses ran almost to the point of maximum deformation, but failed due to excessive distortion of the mesh. Nevertheless, the impact is captured and results are available for comment. Some oscillations are noted in Fig. 15(d) towards the end of the impact, which is explained by the pipe "wrapping" around the impactor.

Fig. 15 shows simulations with FE in the fluid. Equivalent tests with cell-centred FV were conducted and gave very similar results, but these are not shown here for brevity.

6.3. Embedded simulations of filled pipe

Simulations with a Eulerian mesh of either FE or FV for the fluid (now including also the air external to the pipe) combined with a Lagrangian mesh for the structure took longer time since the model has a lot more elements. The search and update of the influence domain can also be costly, but all trouble with building the mesh and mesh update algorithms is effectively eliminated. The fluid mesh is $60\times36\times180$ elements, spanning $500\times300\times1\,500$ mm, and the medium structural mesh (24×78) was initially used for the pipe. Alternatively, a finer pipe mesh (32×104) was also tested with the following refinement of the fluid mesh:

(a) FSCP=0 (b) FSCP=1 (c) FSCP=0, Vofire (d) FSCP=1, Vofire

Figure 16: Diffusion in embedded calculations of pipe I after 85 ms (in a vertical cross-section of the dented zone), with the plots showing fluid density in kg/m^3. Colors indicate fluid density, red is highest.

while using the same amount of fluid elements ($60 \times 36 \times 180$) it was possible to reduce the dimensions of the fluid box without the boundaries disturbing the FSI conditions, so the updated mesh is $350 \times 220 \times 1\,400$ mm. This makes the longest fluid edge about 7.8 mm while the structural shells are 12.5 mm, thus maintaining a finer discretisation of the fluid mesh compared to the structure.

The initial simulation with FE in the fluid and FLSR for the coupling showed that the response was closer to an open than to a closed pipe. This can be due to diffusion which is undoubtedly present as expected (see Fig. 16(a)). This may be ameliorated by coupling the fluid in all spatial directions (FSCP = 1) rather than just along the structure's normal. Obviously, diffusion is still present as seen in Fig. 16(b). The anti-diffusion algorithm called "Vofire" [37] was successfully employed to reduce diffusion (see Figs. 16(c) and 16(d)). From the force-displacement curves in Fig. 17(a), internal pressure is not rising sufficiently to keep the force-level flat throughout the impact, possibly indicating the need for a finer discretisation. As Vofire worked quite well, this option is kept on for the remainder of the embedded calculations.

By using the slightly finer mesh, a flatter force-displacement curve is obtained (see Fig. 17(b)) similar to the full pipes from Fig. 15. Increasing the air contents at the top has the same effect here, although less pronounced, as this fluid mesh is Eulerian and some diffusion will remain even with Vofire. Fig. 17(b) also shows that the flat part of the force-displacement curve is harder to predict. This may be due to the fact that in an embedded calculation, there is no well-defined fluid-structure border, unlike in classical ALE, thereby losing some accuracy. For a confined reservoir, an ALE approach (as far as this can work)

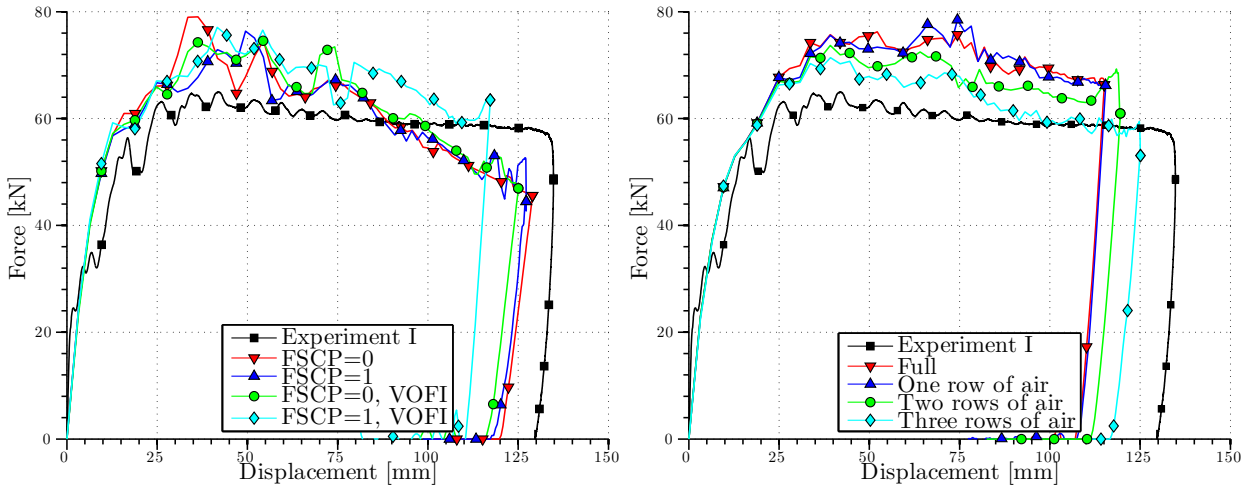

(a) Medium mesh

(b) Fine mesh, FSCP=1, Vofire

Figure 17: Force-displacement curves from embedded simulations of pipe I.

seems to provide better results. If a submerged structure with surrounding fluid was to be modelled, an embedded technique is the natural choice as the Eulerian part of the embedded mesh is easily extended to account for surrounding water as done in [29].

Like in the case of conforming simulations (Section 6.2), equivalent tests to those of Fig. 17 were conducted with cell-centred FV in the fluid and FLSW coupling. Results were very similar to those obtained with FE/FLSR, and are omitted for brevity.

6.4. SPH simulations of filled pipe

Finally, we present simulations performed by the SPH method mentioned in Section 5.2. A first simulation was conducted for the case of an open water-filled pipe (test G), for which a Lagrangian description such as SPH lends itself particularly well. As shown in Fig. 18, SPH is able to represent water overflow at the pipe top in a natural way, without having to use multi-phase material and to discretise an initially empty space, like it would be with FE/FV fluid models. The result in terms of force-displacement curve is also very good, as shown in Fig. 19(a).

Next, a simulation assuming a nominally filled closed pipe (pipe I) is shown in Fig. 20. The pipe was discretised by a uniform mesh of 32×104 shells. Fig. 20(a) shows the initial

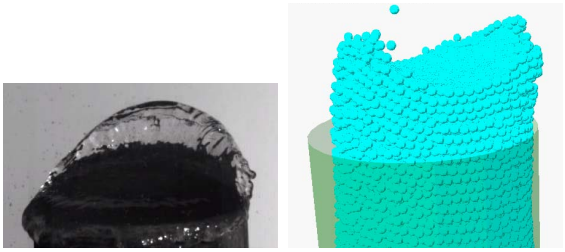

(a) Test G (b) SPH result

Figure 18: SPH simulation of open-filled pipe (G).

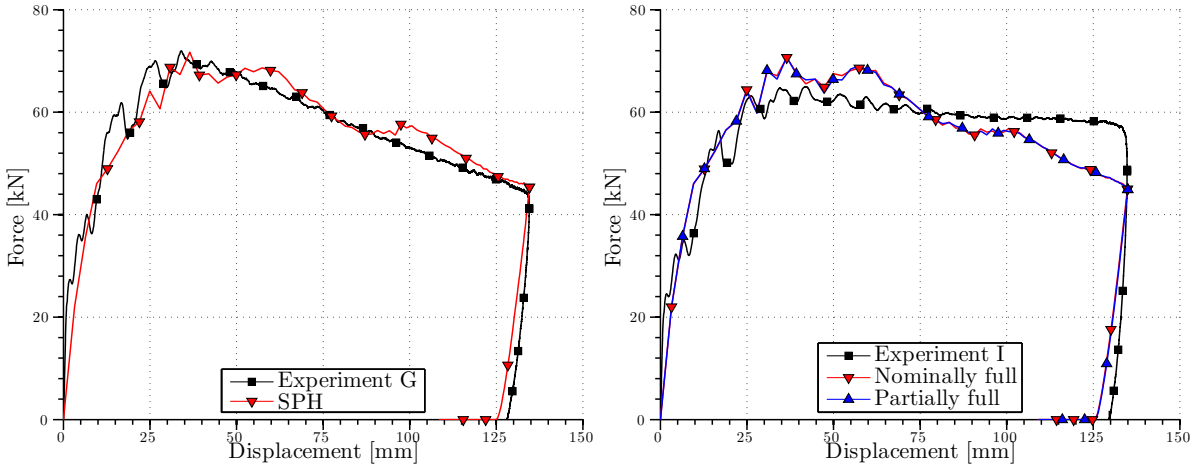

(a) Pipe G (open) (b) Pipe I (closed)

Figure 19: Force-displacement curves from SPH simulations.

SPH mesh near the impacted zone, using particles with a uniform radius of 2.5 mm, while Fig. 20(b) shows the deformed mesh at the instant of maximum deflection (at about 90 ms). Fig. 19(b) shows the contact force vs. displacement of the impactor.

The agreement with the experiment is quite good, with the exception perhaps of the latter part of the curve (for displacements larger than 100 mm). No gross overestimate of the contact force is observed, unlike other simulations with a filled pipe. This is due to the fact that with the standard SPH model available in the computer code it is impossible, in practice, to fill in a pipe perfectly, even in the initial configuration, because all particles are supposed to have the same diameter. Despite the use of an hexagonal close-packed array of (equally-sized) particles some gaps always remain between the particles and the cylinder.

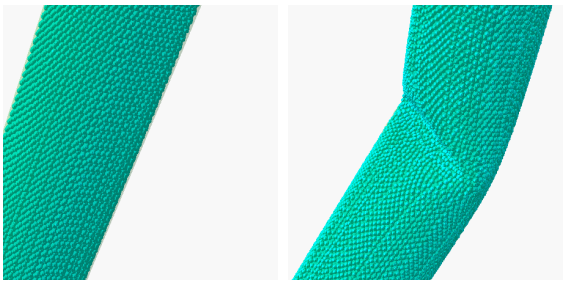

(a) Initial SPH mesh (b) Mesh at 90 ms

Figure 20: SPH for nominally filled and closed pipe (I).

The total mass of the particles was 15.02 kg (for a water density of $\rho = 1\,000$ kg/m^3), while the nominal mass of the water is $M_w = \pi R^2 L \rho = \pi(63.31 \times 10^{-3})^2 \times 1.3 \times 1\,000 = 16.37$ kg, with R the inner tube radius and L the total tube length, including the extensions. To confirm the above conjecture, a second calculation with particles only partially filling the pipe and leaving an empty zone of 25 mm in the upper part of the tube was run. As a matter of fact, this simulation gave very similar results, as seen in Fig. 19(b). Fig. 21 shows the initial SPH mesh for a partially filled pipe, and the mesh after 90 ms. The SPH particles flow nicely to fill the gap after impact.

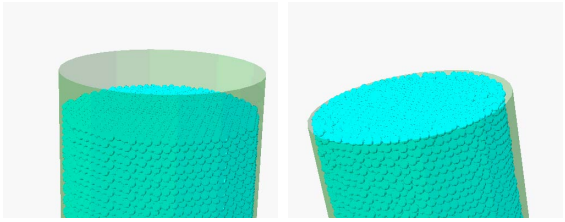

(a) Initial mesh (b) Mesh at 90 ms

Figure 21: SPH simulation of partially filled pipe, showing the top of the pipe.

Another shortcoming of the SPH method in the closed-filled pipe case is that the residual internal pressure in the tube is not correctly predicted (unlike with FE or FV-based models), again due to inaccurate representation of liquid volume near the walls and consequent lack of precision in representing the pressure field along the boundaries of the fluid domain, in contact with the structure. Such drawbacks of the classical SPH method are known from

Table 3: Selected numerical results compared with experiments (see Fig. 6 for legend).

		Pipe A		**Pipe G**		**Pipe I**		
		Exp.	LAGR	Exp.	SPH	Exp.	FSA	FLSR[a]
Stru. mesh		-	32×104	-	32×104	-	32×104	32×104
Fluid els.		-	-	-	169 971	-	33 280	388 800
Rows air		-	-	-	0	-	2	3
d_i	[mm]	170	169	140	140	139	132	129
$d_{\text{N-S}}$	[mm]	60	60	68	67	77	72	71
$L_{\text{N-N}}$	[mm]	1250	1246	1255	1252	1270	1255	1257
h	[mm]	-	-	-	-	14	11	6
F_{peak}	[kN]	71	70	72	72	65	69	71
p	[MPa]	-	-	-	-	5.6[b]	2.4	2.0
CPU	[days]	-	0.09	-	3.01	-	1.03	25.78
Figure no.		5(a)	13(b)	5(a)	19(a)	5(a)	15(b)	17(b)

[a]FLSR calculation is with Vofire and FSCP=1.

[b]Based on analytical estimate.

the literature and are due basically to incomplete neighbourhood of the particles near the boundaries. These aspects are of course much less important in classical SPH applications such as high-speed impact of projectiles, and also in the present case if one considers an open-filled pipe, where very little (if any) internal pressure is built up in the fluid, anyway.

It may be concluded that SPH is a very powerful and versatile method to treat FSI problems: there is no difficulty in representing partially filled vessels and one could easily add the treatment of structural failure, formation of water jets, etc., if needed. However, a drawback of the method in its standard form is the inability to accurately represent a perfectly filled reservoir, whenever this may be of importance. These simulations took about 3 days of CPU time each. A simulation with twice coarser SPH mesh (particle radius of 5 mm, thus 8 times less particles) was attempted to reduce the computer time, but results were not accurate enough. This was expected, since it is well known that SPH methods

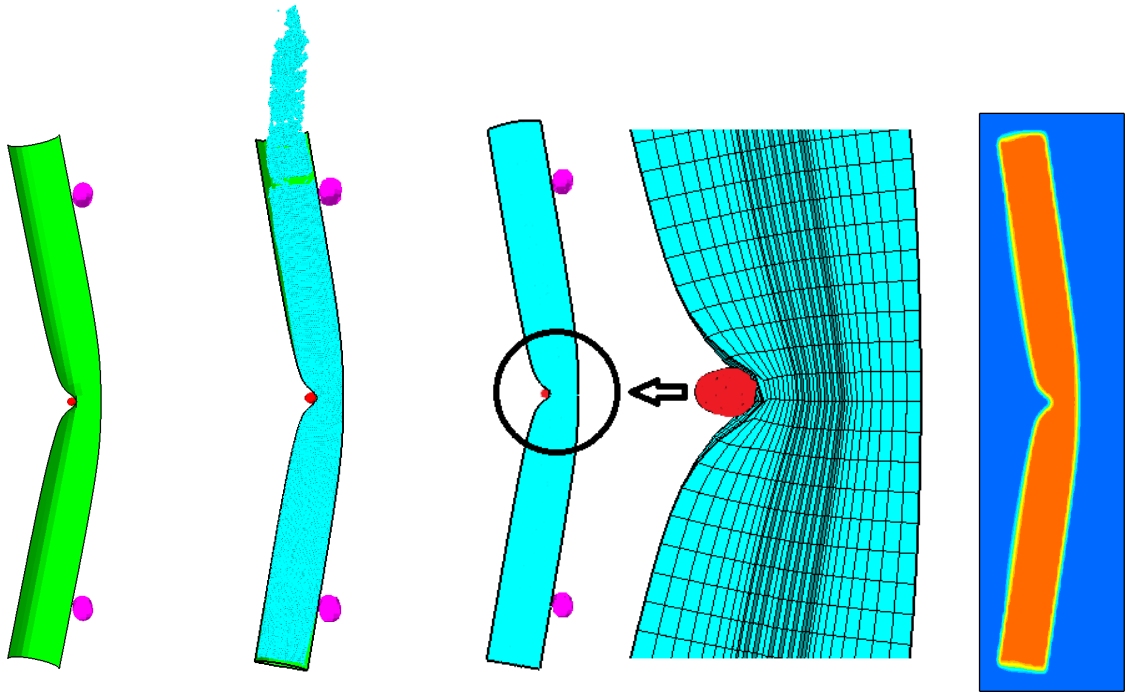

(a) Empty pipe (b) Open-filled, SPH (c) Closed-filled, ALE (d) Closed-filled, embedded

Figure 22: A visual comparison of all the approaches used in the numerical simulations.

require a very fine mesh.

Some selected simulations are compared with experimental data in Table 3, including the estimated pressure from the experiments. The reported CPU times were measured on a normal desktop computer running the sequential (non-parallelised) version of the code.

To summarise, Fig. 22 gives a visual comparison of the various numerical simulation approaches investigated in the present work: (a) the Lagrangian approach used for the empty pipe (test A); (b) the SPH formulation used for the open-filled pipe (test G); (c) the ALE formulation with FSA coupling and (d) the Euler-Lagrange formulation with embedded coupling, used for the closed-filled pipe (test I). Only half of the model, cut vertically through the center, is shown to highlight the internal of the tube. In the right part of Fig. 22(c) the inner ALE fluid mesh around the impacted zone is visible, showing the importance of a robust rezoning algorithm. Fig. 22(d) shows the embedding fluid mesh only, with an isoplot

of the density as in Fig. 16. The water (red) is nicely retained within the confines of the pipe.

7. Discussion and concluding remarks

The X65 steel presented itself as homogeneous and isotropic [12]. A strain rate dependency was found, with a 20% increase of flow stress at 4% true plastic strain for the highest strain rate (830 s^{-1}). The fracture strain, however, appeared unaffected – the difference at quasi-static strain rate and the highest strain rate was less than the standard deviation between the quasi-static tension tests alone.

Impact tests against a simply supported pipe were conducted at about 3.2 m/s and 5.1 m/s. For each velocity, three cases were studied – empty pipes, open water-filled pipes, and closed water-filled pipes. For both velocities, the empty and open water-filled pipes behaved very similarly. As the water is free to flow out during impact, and the mass of the water is small compared to the impacting mass, this is according to intuition.

At an impact velocity of 3.2 m/s, the closed water-filled pipe shows a distinctly different behaviour. The force-displacement curve becomes much flatter with a higher force level during the latter part of the impact. This is attributed to the fact that the water is unable to evacuate the pipe, and pressure starts to build up as the pipe deforms, thereby providing additional resistance to deformation.

The very same tendencies are observed at an impact velocity of 5.1 m/s, but unfortunately the pressure in the pipe became too large for the deformable end cap to accomodate and the weld between the pipe and the end cap ruptured in the experiment (see Fig. 7). At this point, a sudden drop in the force level is observed, plotted in Fig. 5(b). The force-displacement curve has the same shape as for the empty or open water-filled pipe after the rupture, but at a somewhat higher force level. This is most likely caused by the water being forced through a narrow opening at the top rather than being completely free to escape.

Due to these observations, the main focus of the numerical work has been with pipe I (closed water-filled pipe impacted at 3.2 m/s) as it displayed a distinctly different behaviour compared to A and G, and there was no failure in any of the materials.

The total displacement d_i of the pipes impacted at 3.2 m/s was somewhat smaller for the water-filled pipes (140 and 139 mm compared to 170 mm for the empty pipe), suggesting that some resistance is offered by the water as observed by Shah [11]. The cross-sectional deformation was quite different between the closed water-filled pipe and the other two as shown in Table 1. The "diameters" along the impact direction $d_{\text{N-S}}$ were 60, 68 and 77 mm for pipe A, G and I respectively, increasing in accordance with previous observations [9, 11].

All the Lagrangian simulations of impact against empty pipes (A and B) captured the events very well, apart from the coarsest mesh. Increased shell thickness leads to a higher peak force and correspondingly lower deformation as expected, and also noted in [29]. No significant difference in the contact force was found between the nodal and hierarchic pinballs, given a sufficiently fine mesh. It is concluded that the structural part of the experiments is represented with adequate accuracy.

With pipe I as starting point, ALE simulations including the contained fluid were set up. A pipe completely full of water acted too stiffly during impact as seen in Fig. 15. As some air was most likely trapped in the pipe in the experiments, this was also included in the simulations. Fig. 15 shows that by tuning the air volume fraction along with the mesh grade a very good result is obtained.

The same procedure is attempted for the embedded calculations – Fig. 15(b) and 17(b) show the ALE and embedded results respectively. Again quite good results are obtained with the embedded method by coupling the fluid and the structure in all spatial directions (FSCP=1) and with anti-diffusion, although not as accurate as the ALE approach. From Fig. 16 it is evident that the Vofire anti-diffusion algorithm works well as the liquid-gas border is readily identified within three elements or so.

SPH formulation lends itself very well to simulation of open-filled pipes. However, in the case of closed-filled pipes it underestimates the internal fluid pressure build-up due to pipe deformation. A remedy (to be implemented in the future within the code) would consist in ameliorating pressure field representation in SPH particles located near the fluid domain boundaries, where the neighbourhood of such particles is incomplete.

To summarise, the Lagrangian simulations were able to represent the impact against empty pipes well, both in terms of global force-displacement curves and of local deformation. When modelling a confined reservoir of water like for pipe I, a classical ALE approach is the most suited. The embedded method has some diffusion while SPH is inherently unable to fill the volume completely, even with dense hexagonal packing. If fracture and evacuation of water are to be included, modelling becomes more complicated. If using ALE for this, the mesh would have to be extended beyond the geometry of the pipe to accomodate the escaping water. An embedded or an SPH calculation would require no other modification than an accurate fracture criterion. Also, the embedded technique is well suited for treating submerged structures, as the Eulerian fluid mesh can easily be extended to respresent a surrounding liquid as in [29].

Acknowledgements

The present work has been carried out with financial support from SIMLab – Centre for Research based Innovation (CRI) at the Norwegian University of Science and Technology. Thankful acknowledgement is made to Dr. Ing. Håvar Ilstad and Dr. Ing. Erik Levold at Statoil ASA for their contributions and for supplying the test material. Contributions from M.Sc. students Kjetil Slåttedalen, Anders Ørmen, Jo Gaute Fornes and Steffen Gabrielsen are also greatly appreciated. Thanks also to the Joint Research Centre, Ispra, for lending computer power.

References

[1] Statoil ASA, Small gas leak from Kvitebjørn pipeline, Cited 06.01.2014. `http://www.statoil.com/en/NewsAndMedia/News/2008/Pages/gasleakkvitebjorn.aspx`.

[2] N. Jones, R. Birch, Influence of internal pressure on the impact behaviour of steel pipelines, International Journal of Pressure Vessel Technology 118 (1996) 464–471.

[3] DNV, Offshore standard DNV-RP-F111: Interference between trawl gear and pipelines, Det Norske Veritas, 2010.

[4] Petroleumstilsynet, Damage and incidents involving load-bearing structures and pipeline systems, Petroleum Safety Authority Norway, Cited 06.01.2014. http://www.ptil.no/news/damage-and-incidents-involving-load-bearing-structures-and-pipeline-systems-article4306-79.html?lang=en_US.

[5] N. Jones, S. Birch, R. Birch, L. Zhu, M. Brown, An experimental study on the lateral impact of fully clamped mild steel pipes, Proceedings of IMechE, Part E: Journal of Process Mechanical Engineering (1992) 111–127.

[6] K. Chen, W. Shen, Further experimental study on the failure of fully clamped steel pipes, International Journal of Impact Engineering 21 (1998) 177–202.

[7] W. Shen, D. Shu, A theoretical analysis on the failure of unpressurised and pressurised pipelines, Proceedings of the Institution of Mechanical Engineers 216 (E) (2002) 151–165.

[8] C. Ng, W. Shen, Effect of lateral impact loads on failure of pressurised pipelines supported by foundation, Proceedings of the Institution of Mechanical Engineers 220 (E) (2006) 193–206.

[9] N. Jones, R. Birch, Low-velocity impact of pressurised pipelines, International Journal of Impact Engineering 37 (2010) 207–219.

[10] A. Neilson, W. Howe, G. Garton, Impact resistance of mild steel pipes: An experimental study, Safety Experiments and Analysis Group, Safety and Engineering Science Division AEE Winfrith, AEEW – R 2125 (1987).

[11] Q. Shah, Experimental and numerical study on the orthogonal and oblique impact on water filled pipes, International Journal of Impact Engineering 38 (2011) 330–338.

[12] M. Kristoffersen, T. Børvik, I. Westermann, M. Langseth, O. Hopperstad, Impact against X65 steel pipes — An experimental investigation, International Journal of Solids and Structures 50 (2013) 3430–3445.

[13] A. Tijsseling, Fluid-structure interaction in liquid-filled pipe systems: A review, Journal of Fluids and Structures 10 (1996) 109–146.

[14] R. Mohammad, A. Kotousov, J. Codrington, Analytical modelling of a pipe with flowing medium subjected to an impulse load, International Journal of Impact Engineering 38 (2011) 115–122.

[15] V. Longva, S. Sævik, E. Levold, H. Ilstad, Dynamic simulation of subsea pipeline and trawl board pull-over interaction, Marine Structures 34 (2013) 156–184.

[16] Y. Chen, A. Clausen, O. Hopperstad, M. Langseth, Application of a split-Hopkinson tension bar in a mutual assessment of experimental tests and numerical predictions, International Journal of Impact Engineering 38 (2011) 824–836.

[17] A. Hanssen, T. Auestad, T. Tryland, M. Langseth, The kicking machine: A device for impact testing of structural components, International Journal of Crashworthiness 8 (2003) 385–392.

[18] A. Manes, R. Porcaro, H. Ilstad, E. Levold, M. Langseth, T. Børvik, The behaviour of an offshore steel pipeline material subjected to stretching and bending, Ships and Offshore Structures 7 (2012) 371–387.

[19] A. Hanssen, T. Auestad, M. Langseth, T. Tryland, Development of a 3-component load cell for structural impact testing, International Journal of Mechanics and Materials in Design 2 (2005) 15–22.

[20] Z. Marciniak, J. Duncan, S. Hu, Mechanics of sheet metal forming, Oxford: Butterworth-Heinemann, 2002.

[21] G. Gruben, E. Fagerholt, O. Hopperstad, T. Børvik, Fracture characteristics of a cold-rolled dual-phase steel, European Journal of Mechanics A/Solids 30 (2011) 204–218.

[22] K. Rakvåg, N. Underwood, G. Schleyer, T. Børvik, O. Hopperstad, Transient pressure loading of clamped metallic plates with pre-formed holes, International Journal of Impact Engineering 53 (2013) 44–55.

[23] G. Johnson, W. Cook, A constitutive model and data for metals subjected to large strains, high strain rates and high temperatures, Proceedings of the 7^{th} International Symposium on Ballistics (1983) 541–547.

[24] B. Moras, Constitutive Equations of Strain Rate Sensitive Metals for the Automotive Industry, Technical Report, Structural Mechanics Unit, Joint Research Centre, Ispra, Italy, 1999.

[25] R. Hill, The Mathematical Theory of Plasticity, Oxford University Press, 1950.

[26] G. Le Roy, J. Embury, M. Ashby, A model of ductile fracture based on the nucleation and growth of voids, Acta Metallurgica 29 (1981) 1509–1522.

[27] Europlexus user's manual, Joint Research Centre, Cited 30.08.2013. `http://europlexus.jrc.ec.europa.eu/public/manual_pdf/manual.pdf`.

[28] F. Casadei, M. Larcher, N. Leconte, Strong and weak forms of a fully non-conforming FSI algorithm in fast transient dynamics for blast loading of structures, III ECCOMAS Thematic Conference on Computational Methods in Structural Dynamics and Earthquake Engineering, Corfu, Greece (2011).

[29] M. Kristoffersen, F. Casadei, T. Børvik, M. Langseth, G. Solomos, O. Hopperstad, Numerical simulations of submerged and pressurised X65 steel pipes, XII International Conference on Computational Plasticity, Barcelona, Spain (2013).

[30] T. Belytschko, M. Neal, Contact-impact with the pinball algorithm with penalty and Lagrangian methods, International Journal for Numerical Methods in Engineering 31 (1991) 547–572.

[31] S. Giuliani, An algorithm for continuous rezoning of the hydrodynamic grid in Arbitrary Lagrangian Eulerian computer codes, Nuclear Engineering and Design 72 (1982) 205–212.

[32] F. Casadei, J.-P. Halleux, An algorithm for permanent fluid-structure interaction in explicit transient dynamics, Computer Methods in Applied Mechanics and Engineering 128 (1995) 231–289.

[33] F. Casadei, S. Potapov, Permanent fluid-structure interaction with non-conforming interfaces in fast transient dynamics, Computer Methods in Applied Mechanics and Engineering 193 (2004) 4157–4194.

[34] F. Casadei, Fast transient fluid-structure interaction with failure and fragmentation, 8-th World Congress on Computational Mechanics (WCCM8), Venice, Italy (2008).

[35] J. Monaghan, An introduction to SPH, Computer Physics Communications 48 (1988) 89–96.

[36] M. Kristoffersen, T. Børvik, M. Langseth, H. Ilstad, E. Levold, O. Hopperstad, Damage and failure in an X65 steel pipeline caused by trawl gear impact, Proceedings of the ASME 2013 32$^{\text{nd}}$ International Conference on Ocean, Offshore and Arctic Engineering (2013).

[37] V. Faucher, S. Kokh, Extended Vofire algorithm for fast transient fluid-structure dynamics with liquid-gas flows and interfaces, Journal of Fluids and Structures 39 (2013) 102–125.